Genetic signature of prostate cancer mouse models resistant to optimized hK2 targeted α-particle therapy

Mesude Bicak[a], Katharina Lückerath[b,c], Teja Kalidindi[d], Michael E. Phelps[b,1], Sven-Erik Strand[e], Michael J. Morris[f], Caius G. Radu[b,c,g], Robert Damoiseaux[b], Mari T. Peltola[h], Norbert Peekhaus[b], Austin Ho[b], Darren Veach[d,i,j], Ann-Christin Malmborg Hager[j], Steven M. Larson[d,k], Hans Lilja[f,l,m,n,o], Michael R. McDevitt[d,k], Robert J. Klein[a,1], and David Ulmert[b,c,g,p,1]

[a]Department of Genetics and Genomic Sciences, Icahn Institute for Data Science and Genome Technology, Icahn School of Medicine at Mount Sinai, New York, NY 10029; [b]Department of Molecular and Medical Pharmacology, University of California, Los Angeles, CA 90095; [c]Ahmanson Translational Imaging Division, David Geffen School of Medicine, University of California, Los Angeles, CA 90095; [d]Department of Radiology, Memorial Sloan Kettering Cancer Center, New York, NY 10065; [e]Division of Oncology and Pathology, Department of Clinical Sciences, Lund University, 223 81 Lund, Sweden; [f]Genitourinary Oncology Service, Department of Medicine, Memorial Sloan Kettering Cancer Center, New York, NY 10065; [g]Jonsson Comprehensive Cancer Center, David Geffen School of Medicine, University of California, Los Angeles, CA 90095; [h]Department of Biochemistry-Biotechnology, University of Turku, FI-20014 Turun yliopisto, Finland; [i]Radiochemistry and Imaging Sciences Service, Department of Radiology, Memorial Sloan Kettering Cancer Center, New York, NY 10065; [j]Diaprost AB, 223 63 Lund, Sweden; [k]Department of Radiology, Weill Cornell Medical College, New York, NY 10065; [l]Department of Laboratory Medicine, Memorial Sloan Kettering Cancer Center, New York, NY 10065; [m]Department of Translational Medicine, Lund University, 221 00 Lund, Sweden; [n]Nuffield Department of Surgical Sciences, University of Oxford, Headington, OX3 7DQ Oxford, United Kingdom; [o]Department of Surgery, Memorial Sloan Kettering Cancer Center, New York, NY 10065; and [p]Eli and Edythe Broad Center of Regenerative Medicine and Stem Cell Research, University of California, Los Angeles, CA 90095

Hu11B6 is a monoclonal antibody that internalizes in cells expressing androgen receptor (AR)-regulated prostate-specific enzyme human kallikrein-related peptidase 2 (hK2; *KLK2*). In multiple rodent models, Actinium-225–labeled hu11B6-IgG$_1$ ([^{225}Ac]hu11B6-IgG$_1$) has shown promising treatment efficacy. In the present study, we investigated options to enhance and optimize [^{225}Ac]hu11B6 treatment. First, we evaluated the possibility of exploiting IgG$_3$, the IgG subclass with superior activation of complement and ability to mediate FC-γ-receptor binding, for immunotherapeutically enhanced hK2 targeted α-radioimmunotherapy. Second, we compared the therapeutic efficacy of a single high activity vs. fractionated activity. Finally, we used RNA sequencing to analyze the genomic signatures of prostate cancer that progressed after targeted α-therapy. [^{225}Ac]hu11B6-IgG$_3$ was a functionally enhanced alternative to [^{225}Ac]hu11B6-IgG$_1$ but offered no improvement of therapeutic efficacy. Progression-free survival was slightly increased with a single high activity compared to fractionated activity. Tumor-free animals succumbing after treatment revealed no evidence of treatment-associated toxicity. In addition to up-regulation of canonical aggressive prostate cancer genes, such as *MMP7*, *ETV1*, *NTS*, and *SCHLAP1*, we also noted a significant decrease in both *KLK3* (prostate-specific antigen) and *FOLH1* (prostate-specific membrane antigen) but not in *AR* and *KLK2*, demonstrating efficacy of sequential [^{225}Ac]hu11B6 in a mouse model.

hu11B6 | 225Ac | radioimmunotherapy | prostate cancer | hK2

Actinium-225–labeled antibodies and small molecules targeting prostate-specific antigen (PSA) and prostate-specific membrane antigen (PSMA) are currently being evaluated in clinical trials, and reports have already shown promising therapeutic results in prostate cancer (PCa) patients resistant to androgen receptor (AR)-inhibiting drugs (1–3). Unfortunately, toxicities generated by off-target accumulation in radio-sensitive tissues, such as salivary glands and kidneys, is of growing concern (4). In addition, PSMA expression decreases with increasing AR activity and has been shown to be unevenly expressed in metastases (5–7). We have developed an antibody-based platform that targets human kallikrein-related peptidase 2 (hK2), an AR-regulated prostate enzyme, specifically expressed at abundant levels in prostate-derived tissues. In enzalutamide-resistant disease, in which the glucocorticoid receptor drives the AR-pathway, PSMA expression is lost while hK2 is still highly expressed (8). Our group has previously reported on the targeting specificity, efficacy, and biological response of radiolabeled hu11B6 as an

immunotheranostic vehicle. Preclinical evaluations have been carried out in multiple immunodeficient and immunocompetent rodent disease models as well as in nonhuman primates (3, 9–12). In addition, studies of the uptake mechanism have revealed that hu11B6 is internalized by hK2-expressing cells via a mechanism driven by the neonatal Fc receptor (FcRn); while uncomplexed hu11B6 is released from the cell by recycling endosomes after binding to FcRn, the hu11B6–hK2 complex is routed to lysosomes for processing (10). The proximity of the internalized radionuclide-labeled hu11B6 to the nucleus results in efficient cell kill, which is further accelerated by inherent AR and hK2 up-regulation related to DNA repair (3).

In the present report we investigated alternative strategies to further improve the therapeutic efficacy of hu11B6. In the field

www.manaraa.com

Significance

Molecularly targeted α-therapy is an emerging therapeutic option for prostate cancer patients. We previously developed [^{225}Ac]hu11B6, an α-particle–emitting antibody conjugate, which specifically internalizes into prostate cancer cells by binding to human kallikrein-related peptidase 2. Here, we explore methods to enhance its therapeutic efficacy, prospective treatment strategies, and potential resistance mechanisms in preclinical models. We demonstrate that switching the antibody subclass to IgG$_3$ can be applied to radioimmunotherapy and may enhance efficacy. Second, repeat [^{225}Ac]hu11B6 administration is effective, even in tumors relapsing after initial treatment. Third genetic profiling revealed radio-biological mechanisms associated with relapse after α-radioimmunotherapy that could appropriate combination therapies. Our findings support the clinical translation of [^{225}Ac]hu11B6 as a highly effective, urgently needed treatment option for prostate cancer.

of nuclear medicine, the fragment crystallizable (Fc) is commonly ablated to increase blood clearance. However, these modifications also obliterate possibilities to exploit radiolabeled monoclonal antibodies (mAbs) to orchestrate Fc-receptor–activated cytotoxic effects. IgG$_3$ activates complement and Fc-γ receptor (FcγR)-mediated functions more efficiently than other subclasses. We therefore investigated if changing the subclass of hu11B6 from IgG$_1$ to IgG$_3$ could improve therapeutic efficacy. However, wild-type IgG$_3$ has low FcRn binding capacity due to an arginine at amino acid position 435 (R435), abrogating cellular internalization (13). To overcome this, we constructed a H435 (i.e., histidine at amino acid 435) containing a hu11B6 IgG$_3$ allotype, generating hu11B6-IgG$_3$^{R435H}. As another optimization step, we evaluated therapeutic efficacy of a single high activity vs. two lower activity fractions. Finally, we examined the genetic profile of PCa tumors resistant to [^{225}Ac]hu11B6-IgG$_1$ therapy. In summary, while IgG$_3$ has shown increased immunotherapeutic efficacy compared to IgG$_1$ (14–16), no advantage was shown when applied as a radiolabeled compound targeting hK2. Although susceptible to retreatment, tumors relapsing after [^{225}Ac]hu11B6-IgG$_1$ showed up-regulation of several oncogenes related to aggressive disease.

Results

Radiochemistry. The radiochemical yield for the [^{225}Ac]DOTA-hu11B6 product using a one-step labeling method was 60.2 ± 29.3% (n = 5). The product was 98.5 ± 2.0% (n = 5) radiochemically pure and the specific activity was 0.068 Ci/g ± 0.032 Ci/g (2.516 GBq/g ± 1.184 GBq/g; n = 5). The radiochemical yields for the four hu11B6 combinations prepared using a two-step radiolabeling method were as follows: [^{225}Ac]hu11B6-IgG$_1$ (native IgG$_1$), 3.7 ± 2.1% (n = 13); [^{225}Ac]hu11B6-IgG$_1$^{H435A} (H435A mutant IgG$_1$), 3.1 ± 1.0% (n = 3); [^{225}Ac]hu11B6-IgG$_3$ (wild-type IgG$_3$), 11.0% (n = 1); and [^{225}Ac]hu11B6-IgG$_3$^{R435H} (R435H mutant IgG), 9.1% (n = 1). The radiochemical purity was as follows: Native IgG$_1$, 99.3 ± 0.51%; H435A mutant IgG$_1$, 99.7 ± 0.21%; wild-type IgG$_3$, 99.8%; and R435H mutant IgG$_3$, 99.8%. The specific activity was as follows: Native IgG$_1$, 0.079 Ci/g ± 0.055 Ci/g (2.923 GBq/g ± 2.035 GBq/g); H435A mutant IgG$_1$, 0.059 Ci/g ± 0.018 Ci/g (2.183 GBq/g ± 0.666 GBq/g); wild-type IgG$_3$, 0.068 Ci/g (2.516 GBq/g); and R435H mutant IgG$_3$, 0.066 Ci/g (2.442 GBq/g). Comparable radiochemical purity and specific activities were achieved in either process. Radiochemical yields and specific activities were similar to those observed with other clinically used, intact IgG proteins, such as [^{225}Ac]Lintuzumab. The radiochemical purities of ∼99% that we achieved are suitable for clinical specifications (17–19). The KD of [^{225}Ac]

DOTA-hu11B6, DOTA-hu11B6, and hu11B6 for recombinant hK-2 was 16.7, 16.3, and 15.0 nM, respectively, and indicated that the radiometal chelate 1,4,7,10-tetraazacyclododecane-1,4,7,10-tetraacetic acid (DOTA) conjugation and subsequent ^{225}Ac-radiolabeling did not affect affinity of the antibody for target analyte.

The Impact of IgG Subclass on [^{225}Ac]hu11B6 Pharmacokinetics. Compared to wild-type [^{225}Ac]hu11B6-IgG$_3$, significantly (P = 0.0139 for all) higher target tissue uptakes were noticed in the genetically modified mouse models (GEMM) for FcRn optimized [^{225}Ac]hu11B6-IgG$_3$^{R435H}. In the ventral, anterior, and dorsal/lateral prostate lobes of Hi-*Myc* × pb_*KLK2* mice, percent injected activity per gram (%IA/g; ± SD) of [^{225}Ac]hu11B6-IgG$_3$^{R435H} were 7.75 ± 1.99, 3.60 ± 1.14, and 7.08 ± 3.65, while %IA/g (±SD) [^{225}Ac]hu11B6-IgG$_3$ were 2.48 ± 0.50, 1.03 ± 0.17, and 0.80 ± 0.26, respectively, at 10 d postinjection (Fig. 1*A*). Lymph node carcinoma of the prostate (LNCaP)-AR tumor models led to similar findings; [^{225}Ac]hu11B6-IgG$_3$^{R435H} showed significantly (P = 0.1653 at 4 h postinjection [hpi], P = 0.0003 at 72 hpi, P = 0.0132 at 240 hpi) higher tumor uptake compared to [^{225}Ac]hu11B6-IgG$_3$, 8.45 ± 4.28 and 0.86 ± 0.79%IA/g (±SD), respectively, at 10 d postinjection (Fig. 1*B*). As expected, enhancement of FcRn binding resulted in a strong trend toward longer blood circulation time of [^{225}Ac]hu11B6-IgG$_3$^{R435H} (vs. [^{225}Ac]hu11B6-IgG$_3$) in both GEMM (P = 0.0736 at 240 hpi) and tumor xenograft models (P = 0.0013 at 4 hpi, P = 0.0552 at 72 hpi, P > 0.9999 at 240 hpi). Compared to the IgG$_1$ variant, [^{225}Ac]hu11B6-IgG$_3$^{R435H} showed significantly lower target tissue accumulation (LNCaP-AR, P = 0.0098 and GEMM, P = 0.0299 for IgG3^{R435H} at 240 hpi vs. IgG$_1$ at 400 hpi) and shorter retention time in blood (LNCaP-AR, P = 0.0056 and GEMM, P = 0.4238 for IgG3^{R435H} at 240 hpi vs. IgG$_1$ at 400 hpi) at the final distribution timepoint, while significantly higher (P ≤ 0.0174 for all in both models) accumulation of [^{225}Ac]hu11B6-IgG$_3$^{R435H} was noted in Ig degrading organs (i.e., liver and spleen).

The Impact of IgG Subclass on [^{225}Ac]hu11B6 α-Radioimmunotherapy (RIT) in LNCaP-AR Subcutaneous Xenografts. Mice with LNCaP-AR subcutaneous xenografts were randomized to receive (*A*) [^{225}Ac]hu11B6-IgG$_1$ (n = 5), (*B*) [^{225}Ac]hu11B6-IgG$_1$^{H435A} (IgG$_1$ with inhibited FcRn-coupled cellular processes by exchanging histidine 435 to an alanine) (n = 5), (*C*) [^{225}Ac]hu11B6-IgG$_3$^{R435H} (n = 5), or (*D*) [^{225}Ac]hu11B6-IgG$_3$ (n = 5). [^{225}Ac]hu11B6 constructs based on FcRn complexing Ig-subforms resulted in significantly better treatment outcomes (*SI Appendix*, Fig. S1). Kaplan–Meier analysis of the four treatment groups showed median survival of 18.43 (*A*), 9.14 (*B*), 11.42 (*C*), and 7.86 (*D*) weeks after administration of 300 nCi (11 kBq), respectively (*A* vs. *B*, P < 0.0001; *C* vs. *D*, P = 0.0020; *A* vs. *C*, P = 0.0536) (Fig. 2*A*). Assessment of volumetric effects showed that mice treated with [^{225}Ac]hu11B6-IgG$_3$^{R435H} had reduced tumor growth kinetics compared to [^{225}Ac]hu11B6-IgG$_3$ (Fig. 2*B*). However, [^{225}Ac]hu11B6-IgG$_1$ outperformed [^{225}Ac]hu11B6-IgG$_3$^{R435H} (Fig. 2*C*); at the conclusion of the study, half of the animals treated with the specific and internalizing [^{225}Ac]hu11B6-IgG$_1$ drug were alive, while only one animal was alive in the group that received [^{225}Ac]hu11B6-IgG$_3$^{R435H}.

The Impact of IgG Subclass on [^{225}Ac]hu11B6 α-RIT in Immunocompetent PCa GEMM. Forty- to 55-wk-old hK2-expressing Hi-Myc GEMM were randomized to receive (*A*) [^{225}Ac]hu11B6-IgG$_1$ (n = 7), (*B*) [^{225}Ac]hu11B6-IgG$_1$^{H435A} (n = 7), (*C*) [^{225}Ac]hu11B6-IgG$_3$^{R435H} (n = 7), (*D*) [^{225}Ac]hu11B6-IgG$_3$ (n = 7), or (*E*) nonspecific [^{225}Ac]IgG$_1$ (n = 5). Kaplan–Meier analysis of these five treatments showed median survival of undefined (*A*; >50% of the cohort had survived with [^{225}Ac]hu11B6-IgG$_1$), 8.71 (*B*), 15.71 (*C*), 12.0 (*D*), and 8.72 (*E*) wk after administration of 300 nCi (11 kBq), respectively (*A* vs. *B*, P = 0.0020; *C* vs. *D*, P = 0.0576; *A* vs. *C*,
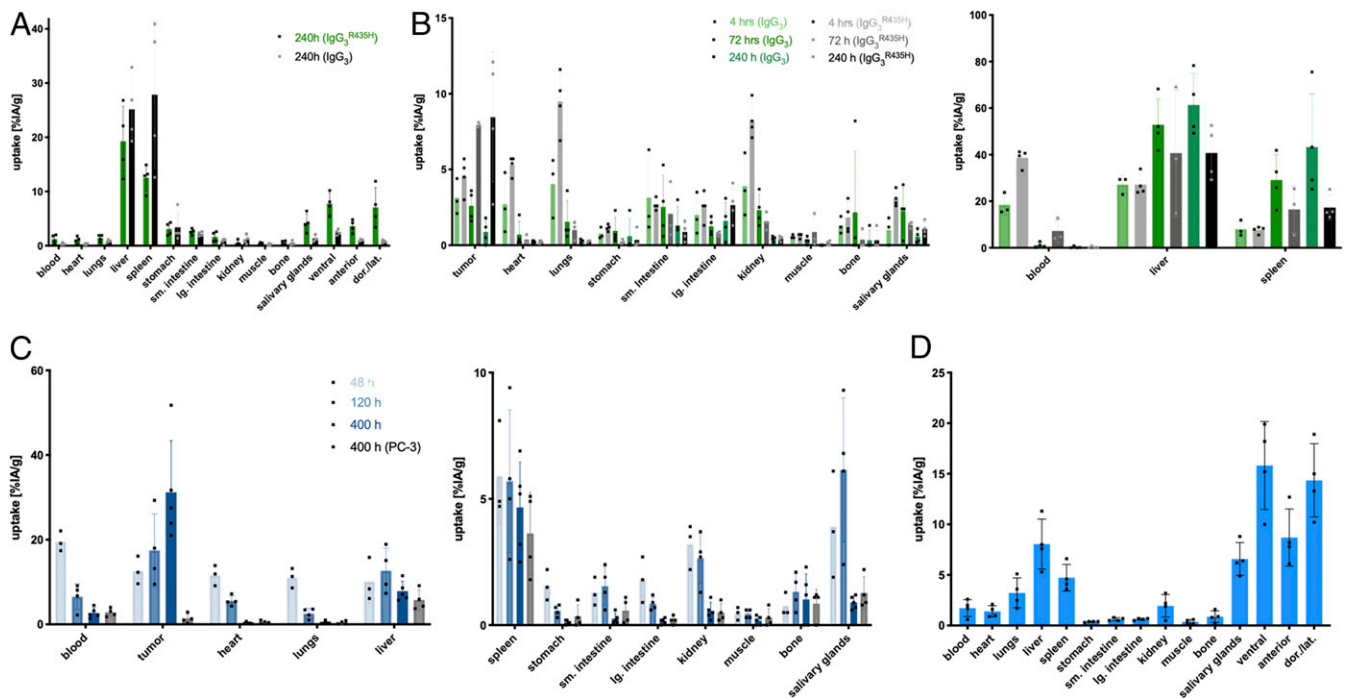
Fig. 1. Biodistribution of [^{225}Ac]hu11B6. (*A* and *B*) Favorable biodistribution of FcRn optimized [^{225}Ac]hu11B6-IgG$_3$^{R435H}. Mice received 300 nCi (11 kBq) [^{225}Ac]hu11B6-IgG$_3$ or [^{225}Ac]hu11B6-IgG$_3$^{R435H}. Organs were collected at indicated time points (h) and specific uptake (%IA/g) was determined with a γ-counter. (*A*) Hi-Myc_*KLK2* GEMM. (*B*) LNCaP-AR xenografts. [^{225}Ac]hu11B6-IgG$_3$ treatment: Light green, 4 h; middle green, 48 h; dark green, 240 h. [^{225}Ac]hu11B6-IgG$_3$^{R435H}: Light gray, 4 h; middle gray, 48 h; dark gray, 240 h. For better visualization, biodistribution data in the LNCaP-AR model are shown in two separate graphs with different *y*-axis scales. (*C* and *D*) Biodistribution of [^{225}Ac]hu11B6-IgG$_1$, labeled using a one-step protocol. Mice received 300 nCi (11 kBq) [^{225}Ac]hu11B6-IgG$_1$. Organs were collected at indicated time points and specific uptake (%IA/g) was determined in a γ-counter. (*C*) LNCaP-AR and PC-3 xenografts. LNCaP-AR are shown in blue: Light blue, 48 h; middle blue, 120 h; dark blue, 400 h. PC-3 are shown in gray (400 h). For better visualization, biodistribution data are shown in two separate graphs with different *y*-axis scales. (*D*) Hi-Myc_*KLK2* GEMM, 400-h time point. Columns and bars represent the mean ± SD (*n* = 5 miceg per group). Individual values are shown as black squares. Time indicates time postradioligand injection. dor./lat., dorsal and lateral prostate; lge. int., large intestine; sm. Intestine, small intestine.

P = 0.1197) (Fig. 2*D*). At the end of the study, four of seven (57%) GEMM were alive in group *A* but only one of seven (14%) in group *C*. These data indicate that an IgG$_1$-based hK2 targeting compound is more effective than IgG$_3$^{R435H} when applied for α-particle RIT. Therapeutic effect by ineffective FcRn-binding compounds (*B*, *D*) were not significantly different from nonspecific [^{225}Ac]IgG$_1$ (*B* vs. *E*, *P* = 0.9738; *D* vs. *E*, *P* = 0.5726), showing that efficacy is dependent on a combination of specific targeting and cellular internalization.

Pharmacokinetics of [^{225}Ac]hu11B6-IgG$_1$, Labeled Using a One-Step Protocol, in Subcutaneous PCa Xenografts and Immunocompetent PCa GEMM. The one-step labeling protocol based on preconjugated hu11B6 was developed to facilitate clinical translation. Biodistribution of [^{225}Ac]hu11B6 was studied in LNCaP-AR (*KLK2$^+$*) subcutaneous xenografts at 48, 120, and 400 hpi, in PC3 (*KLK2$^-$*) subcutaneous xenografts at 400 hpi and in 15- to 30-wk-old hK2-expressing Hi-Myc GEMM at 400 hpi. As expected, uptake of [^{225}Ac]hu11B6 increased over time in LNCaP-AR tumors and uptake at 400 hpi was significantly
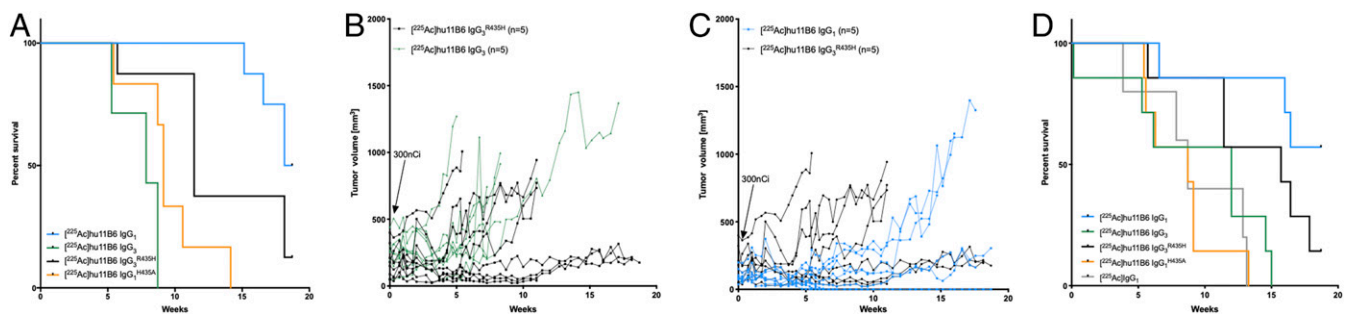
Fig. 2. The impact of IgG subclass on [^{225}Ac]hu11B6 α-radioimmunotherapy. (*A*–*C*) Mice with LNCaP-AR subcutaneous xenografts were randomized to receive 300 nCi (11 kBq) [^{225}Ac]hu11B6-IgG$_1$ (*n* = 5; blue), [^{225}Ac]hu11B6-IgG$_1$^{H435A} (*n* = 5; orange), [^{225}Ac]hu11B6-IgG$_3$^{R435H} (*n* = 5; black), or [^{225}Ac]hu11B6-IgG$_3$ (*n* = 5; green). (*A*) Kaplan–Meier curves for survival. (*B*) Tumor volumes in individual mice following treatment with IgG$_3$ or IgG$_3$^{R435H} antibodies, respectively. (*C*) Tumor volumes in individual mice following treatment with IgG$_1$ or IgG$_1$^{H435A} antibodies, respectively. (*D*) Kaplan–Meier curves for survival of Hi-Myc_*KLK2* GEMM following treatment with 300 nCi (11 kBq) [^{225}Ac]hu11B6-IgG$_1$ (*n* = 7; blue), [^{225}Ac]hu11B6-IgG$_1$^{H435A} (*n* = 7; orange), [^{225}Ac]hu11B6-IgG$_3$^{R435H} (*n* = 7; black), [^{225}Ac]hu11B6-IgG$_3$ (*n* = 7; green), or nonspecific [^{225}Ac]IgG$_1$ (*n* = 5; gray).

($P = 0.0020$) higher than in PC3 tumors at the same time-point (Fig. 1C). In GEMM, the highest specific uptake of $[^{225}Ac]$hu11B6 was found in prostate lobes (Fig. 1D). In summary, the biodistribution profile of one-step–labeled $[^{225}Ac]$hu11B6 closely resembled our previously published results based on the two-step–labeled $[^{225}Ac]$hu11B6 compound (3). Therefore, the one-step labeling protocol was used for all further studies.

Comparison of hK2 Expression Levels in Mouse Models and Human Prostate Tissues. As a result of differences in *KLK2* expression, higher uptake of $[^{225}Ac]$hu11B6 was found in LNCaP-AR tumors compared to uptake in the prostate lobes of Hi-Myc GEMM (10, 11). Average concentrations of hK2 (nanogram) per total protein (milligram) in lysates of ventral, anterior, and dorsal/lateral prostate lobes collected from randomly selected treatment naïve 20-wk-old Hi-Myc GEMM ($n = 4$) were 0.73 ± 0.06, 4.5 ± 0.17, and 1.06 ± 0.37 ng/mg (average for all prostate lobes combined, 2.1 ± 2.1 ng/mg), while LNCaP-AR tumors ($n = 4$) expressed 7.4 ± 2.66 ng/mg. To investigate how the hK2 levels in mice compared with those in humans, hK2 expression was evaluated in 167 human prostate tissue samples obtained from a previously reported cohort of 84 patients (20, 21). Average hK2 levels were 101.6 ± 84.7 ng/mg (*SI Appendix*, Fig. S2) and, thus, ~50 times higher than in the Hi-MYC GEMM.

Therapeutic Efficacy of Fractionated vs. Single Activity $[^{225}Ac]$ hu11B6-IgG$_1$ α-RIT. Bilaterally inoculated LNCaP-AR subcutaneous xenografts were used in both treatment studies. Therapeutic effects were monitored by tumor size (caliper measurements) and assessment of PSA in blood. In the fractionated treatment experiment, animals ($n = 20$) were randomized to receive 300 nCi (11 kBq) $[^{225}Ac]$hu11B6 ($n = 10$) or no treatment ($n = 10$). Previously treated mice were given a second injected activity (300 nCi; 11 kBq) 20 wk after the first treatment. Tumors were either fully eradicated or substantially reduced after each treatment round; five of eight (63%) and two of five (40%) tumors relapsed after the first activity and second activity administration, respectively (*SI Appendix*, Fig. S3A). In the single high-activity treatment experiment, xenografts ($n = 20$) were randomized to receive a single activity 600 nCi (22 kBq) of $[^{225}Ac]$hu11B6 ($n = 10$) or no treatment ($n = 10$). All tumors were eradicated (tumors not palpable and PSA not detectable); during the study period, only one of six (17%) tumors relapsed (*SI Appendix*, Fig. S3B). Mice that had lost weight ($\geq 20\%$ weight loss) at the end of the high-activity study were killed and sent for autopsy evaluation. These reports concluded age-related macroscopic and histopathologic but no treatment-related pathological changes.

When comparing fractionated vs. single activity treatment, neither was associated with toxicity; body weights did not significantly decrease after treatment administration ($2\times$ 300 nCi group, $P \geq 0.0550$; $1\times$ 600 nCi group, all $P \geq 0.7598$; one-way ANOVA with Tukey test to control for multiple comparisons) (*SI Appendix*, Fig. S4). Median survival was not reached (80% of the cohort had survived at the conclusion of the study) following 600 nCi (22 kBq), whereas $2\times$ 300 nCi ($2\times$ 11 kBq) resulted in a median survival of 40.3 wk after the first treatment ($P = 0.3186$ vs. high-activity) (Fig. 3 C and D).

Transcriptome Sequencing. The transcriptome of tumors relapsing after two cycles $[^{225}Ac]$hu11B6 (vs. untreated control tumors, $n = 3$ per group) was profiled (22). RNA sequencing identified 58,828 genes, of which 1,644 (2.8%; 512 up-, 1,132 down-regulated) were differentially expressed in relapsing tumors. Among the differentially expressed genes (DEG), genes associated with aggressive PCa, such as *MMP7 (matrix metalloprotease 7)*, *ETV1 (ETS translocation variant 1)*, *NTS (neurotensin)*, *TMEFF2*

(transmembrane protein with EGF-like and two follistatin-like domains 2), and *SCHLAP1 (SWI/SNF complex antagonist associated with prostate cancer 1)*, and androgen repressed genes, such as *PMP22 (peripheral myelin protein 22)*, *CAMK2N1 (calcium/calmodulin-dependent protein kinase II inhibitor 1)*, and *UGT2-B17UDP (glucuronosyltransferase family 2 member B17)*, were significantly up-regulated. In contrast, several AR-regulated genes—for example, *KLK3*, *FOLH1*, *PMEPA1 (prostate transmembrane protein, androgen induced 1)*, and *SPOCK1 (Testican-1)*—were down-regulated or remained unchanged: *KLK2*, *TMPRSS2 (transmembrane serine protease 2)*, *LONRF1 (LON peptidase N-terminal domain and RING finger protein 1)*, *KCNN2 (small conductance calcium-activated potassium channel protein 2)*. Expression of *AR* itself was comparable in treated and untreated tumors (Table 1). Fig. 4 gives an overview of all DEGs and Tables 2 and 3 summarize the top 10 up-regulated and down-regulated genes.

Discussion

Recently approved drugs that target AR signaling, such as abiraterone and enzalutamide, have rapidly become standard therapies for advanced-stage PCa (23, 24). Initial responses are usually observed, but in an absolute majority of these patients, reactivation of the AR-pathway inevitably occurs within 6 to 12 mo. An alternative treatment option is to target tumors using radiolabeled antibodies or small molecules, a technology that is highly dependent on the specificity of the vehicle and target expression in nonmalignant tissues. We have developed an antibody-based platform that targets hK2, an enzyme that is prostate tissue-specific and under direct regulation of AR, the central driver of prostate adenocarcinoma. Our lead antibody, hu11B6, has been thoroughly evaluated for tumor detection and monitoring of disease activity by positron emission tomography and single-photon emission computed tomography (10, 12). We have reported that hu11B6 can be applied for RIT applications (3, 9, 11). In the present report we aimed to evaluate previously untested and innovative methods that could further increase efficacy. First, we evaluated if therapeutic efficacy could be improved by altering the Fc-subclass. Second, we assessed the impact of dosing strategies. Finally, to determine radio-biological mechanisms that could appropriate combination therapies or elucidate potential drug resistance, we genetically profiled tumors that relapsed after prolonged treatment.

Induction of DNA damage, tumor cell death, and modulation of tumor microenvironment are the main effects of ionizing radiation to reduce tumor masses, but also to effectuate the immune system (25). Therefore, we investigated if the therapeutic efficacy of $[^{225}Ac]$hu11B6 could be improved by exploiting the complement-, and FcγR-binding capacities of the mAb. We constructed an Fc-substituted hu11B6, from IgG$_1$-Fc to IgG$_3$-Fc. Compared to IgG$_1$, wild-type IgG$_3$ has an arginine instead of a histidine at amino acid position 435. Although both residues are positively charged, arginine does not deprotonate at neutral pH, resulting in a less pH-dependent binding to FcRn. To rescue FcRn-mediated internalization, we introduced a histidine at amino acid position 435 (26), generating a hu11B6-IgG$_3$-R435H. Indeed, this optimization is critical as almost no effect was noted with $[^{225}Ac]$hu11B6-IgG$_3$, while $[^{225}Ac]$hu11B6-IgG$_3$-R435H produced a relatively potent therapeutic outcome. Biodistribution in immunodeficient tumor models and immunocompetent GEMM indicated that $[^{225}Ac]$hu11B6-IgG$_3$-R435H is less stable than its IgG$_1$ counterpart; significantly higher uptake in Ig-degrading organs were noted. This is probably due to the long hinge region of IgG$_3$, which is more prone to proteolytic degradation (27).

Based on our results, $[^{225}Ac]$hu11B6-IgG$_3$-R435H did not show any therapeutic advantage over $[^{225}Ac]$hu11B6-IgG$_1$. However, the lack of increased efficacy could be due to critical differences between mouse and human FcγR networks. For
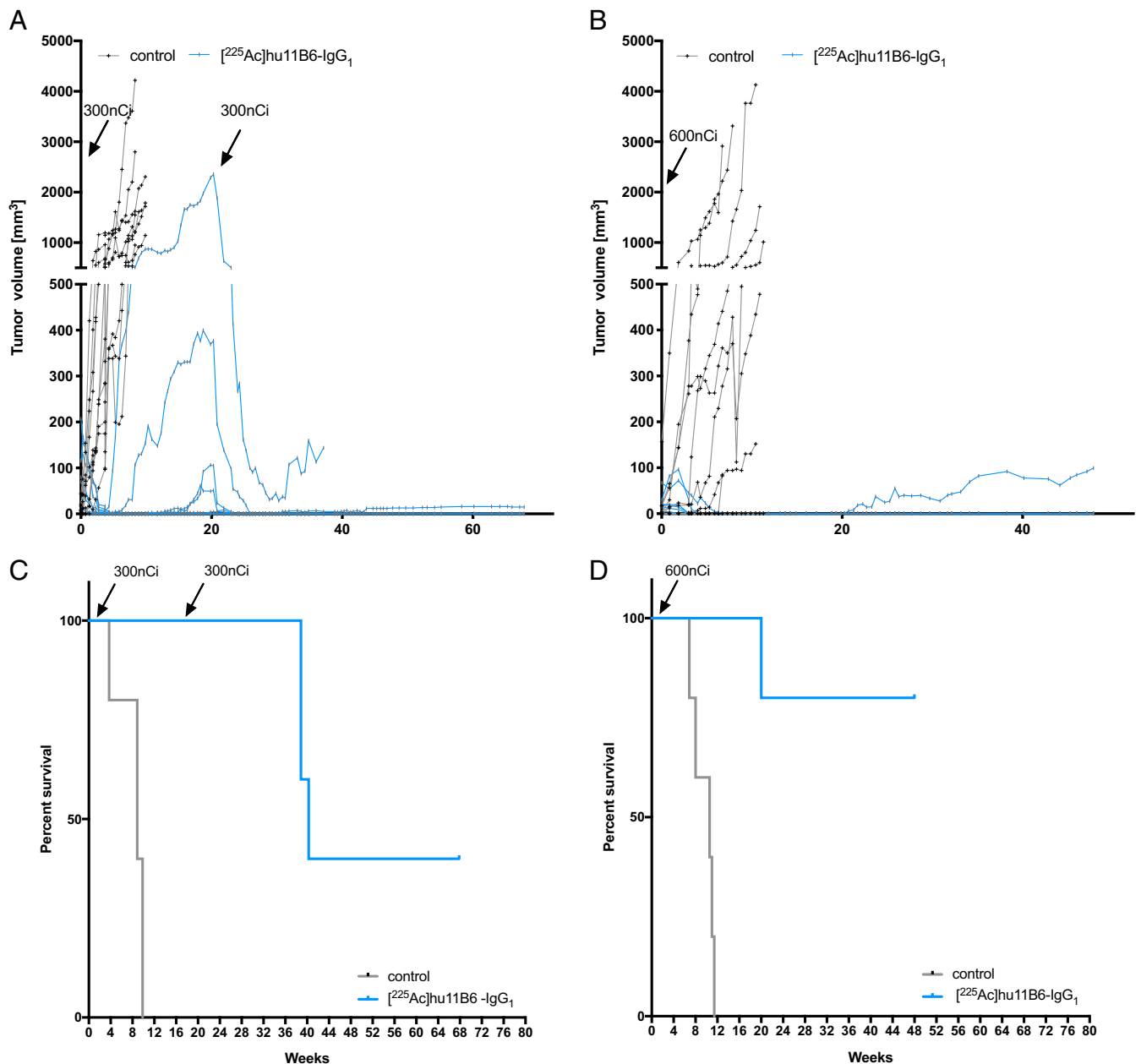
Bicak et al.

MEDICAL SCIENCES

Fig. 3. Therapeutic efficacy of fractionated vs. single high-dose [^{225}Ac]hu11B6-IgG$_1$ α-radioimmunotherapy. Mice with LNCaP-AR subcutaneous xenografts (*n* = 5 mice per group) received 2× 300 nCi (2× 11 kBq; ~4.5 mo apart) (*A* and *C*) or 1× 600 nCi (22 kBq) (*B* and *D*) [^{225}Ac]hu11B6-IgG$_1$ (blue; vs. untreated, black). (*A* and *B*) Tumor volumes of treated and control mice. (*C* and *D*) Kaplan–Meier analysis of survival of treated and control mice.

example, mouse natural killer (NK) cells express mFcγRIII, while human NK cells express hFcγRIIIA. hFcγRIIIA is a key mediator of antibody therapy in humans, while mFcγRIII only modestly contributes to mAb efficacy (28, 29). Therefore, experiments based on GEMM expressing human FcγRs would be needed in order to fully elucidate whether RIT efficacy can be enhanced by using Fc-engineered mAbs. Our approach of exploiting Fc-engineered mAbs for RIT is unique. In the field of nuclear medicine, the Fc region has been viewed as redundant and various Fc-edited antibody-like platforms have been invented (30). Omitting the Fc-region decreases the half-life of the antibody by escaping FcRn interaction and permitting renal clearance. However, Fc contains motifs for activation of both effector immune cells and the classic pathway of the complement (C1q). One of the most important breakthroughs in the field of

immunology during the last two decades is the discovery and characterization of the Fc-portion interaction with FcγR that orchestrates mAb-dependent cellular cytotoxicity through cytotoxic effects via agonistic and antagonistic binding (31). The specific FcγR engaged by a given Fc domain is dictated by Fc structure, which is determined by the IgG subclass. An example of the multifaceted therapeutic activity are checkpoint-inhibitor mAbs (e.g., anti-CTLA4) that mediate antitumor activity by altering the composition and functional activity of leukocytes within the tumor microenvironment. However, the therapeutic action is also an effect of the capacity of the mAb to activate FcγR-expressing macrophages within the tumor microenvironment (32). Radiation has been shown to induce immunemodulatory effects. Both preclinical and clinical studies have shown that radiation enhances the activity of immune checkpoint

www.manaraa.com

Table 1. Differentially regulated genes associated with PCa and AR signaling

Gene name	Fold-change (log$_2$)	P value	Adjusted P value
AR	−0.16	0.3125	0.89
Canonical aggressive PCa genes			
MMP7	7.86	0.00E+00	0.00E+00
ETV1	10.58	0.00E+00	0.00E+00
NTS	11.76	0.00E+00	0.00E+00
SCHLAP1	−12.18	3.20×10^{-150}	3.39×10^{-147}
Androgen-repressed genes			
CAMK2N1	−6.24	4.17×10^{-150}	4.22×10^{-147}
UGT2B17	−3.80	4.67×10^{-45}	5.43×10^{-43}
PMP22	1.57	1.40×10^{-5}	8.96×10^{-5}
AR-regulated genes			
TMEFF2	7.32	1.08×10^{-273}	4.00×10^{-234}
PMEPA1	−1.54	2.34×10^{-20}	2.35×10^{-18}
KLK3	−1.68	1.95×10^{-16}	1.46×10^{-14}
FOLH1	−0.82	4.00×10^{-7}	9.85×10^{-6}
SPOCK1	0.82	2.44×10^{-4}	1.17×10^{-3}
KLK2	−0.44	0.0183	0.12
TMPRSS2	−0.10	0.5442	1.00
LONRF1	0.21	0.3803	0.5191
KCNN2	0.16	0.2955	0.4319

blockers and thereby promotes systemic antitumor responses (33). The capacity of radiation therapy to promote immunomodulatory effects is now the subject of intense scientific and clinical investigation. Based on these observations, a radiolabeled full-sized mAb might have the unique capacity to target its antigen while inducing immune-modulatory effects and activate Fc receptor-mediated cytotoxicity.

Although a single high activity may deliver an optimal absorbed dose to kill a larger fraction of tumor cells, fractionated therapy could offer the advantage of lower myelotoxicity and prolonged tumor response. In accordance with previous studies based on [^{177}Lu]hu11B6, results showed that the therapeutic effect of [^{225}Ac]hu11B6 is absorbed dose-dependent; fewer tumors relapsed in mice treated with a higher activity (11, 34). All of our previous evaluations of [^{225}Ac]hu11B6-RIT studies were based on evaluation of a single activity. In the present study, [^{225}Ac]hu11B6 treatment was repeated when several mice had

relapsed, and relapsed tumors had progressed to a significant volume. Based on tumor and PSA measurements, we did not notice any signs of resistance to treatment when repeated. To retrieve more biologically relevant data, the transcriptome of tumors progressing after [^{225}Ac]hu11B6 were evaluated by RNA sequencing. Although the tumor material posttreatment was limited, since only few tumors relapsed and analysis was only based on a single tumor model, the material displays a unique profile. We have previously reported that early effects (400 h after treatment initiation) of [^{225}Ac]hu11B6 RIT include DNA-repair–associated AR-induction similar to external beam therapy, which resulted in increased expression of hK2 and PSA, while PSMA decreased (3). In the present study, we expanded these finding to tumors relapsing several months after [^{225}Ac]hu11B6 treatment. Compared to treatment-naïve tumors, relapsing tumors harbored an altered expression profile of downstream AR-governed biomarkers. Although AR expression
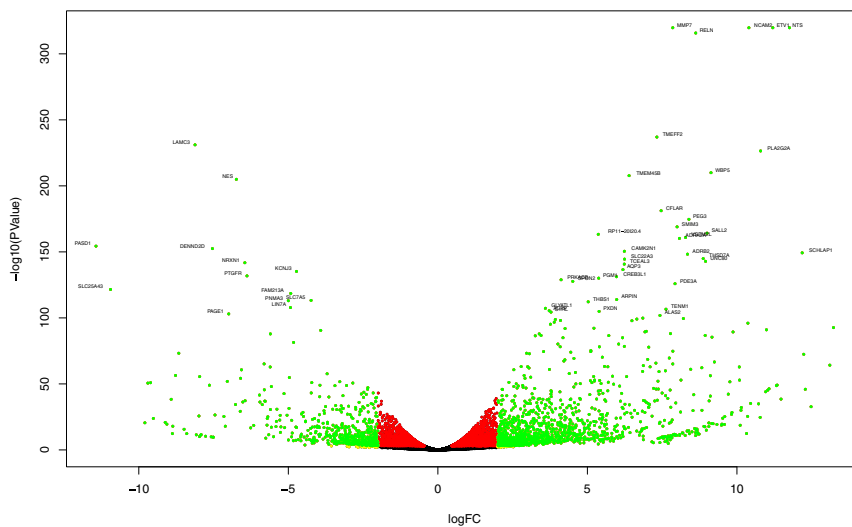

Fig. 4. Summary of the RNA-sequencing results by volcano plot representation of DEGs. The *x* axis shows log$_2$ fold-changes in expression and the *y* axis the log$_{10}$ *P* values of a gene being differentially expressed. Top 50 DEGs are labeled. Green dots represent DEGs with *P* < 0.001 and absolute value of log$_2$ fold-change > 2; yellow dots represent those with only absolute value of log$_2$ fold-change > 2; red dots represent those with only *P* < 0.001.

Bicak et al.

Table 2. Top 10 up-regulated genes at relapse after treatment with [^{225}Ac]hu11B6-IgG$_1$

Gene name	Fold-change (log$_2$)	P value	Adjusted P value
MMP7	7.86	0.00E+00	0.00E+00
NCAM2	10.54	0.00E+00	0.00E+00
ETV1	10.58	0.00E+00	0.00E+00
NTS	11.76	0.00E+00	0.00E+00
TMEFF2	7.32	1.08×10^{-273}	4.00×10^{-234}
PLA2G2A	10.79	3.46×10^{-227}	9.62×10^{-224}
WBP5	9.13	1.01×10^{-210}	2.49×10^{-207}
TMEM45B	6.39	1.78×10^{-208}	3.96×10^{-205}
CFLAR	7.47	6.56×10^{-182}	1.22×10^{-178}
PEG3	8.40	2.22×10^{-175}	3.80×10^{-172}

remained intact, some of the key AR governed genes (FOLH1, KLK3, PMEPA1, and SPOCK1) were down-regulated, while others (KLK2 and TMPRSS2, LONRF1, KCNN2) remained unchanged. Conversely, some of the androgen-repressed genes were up-regulated (PMP22, CAMK2N1, and UGT2B17). Interestingly, these findings bear a resemblance to the genetic changes reported in glucocorticoid receptor-driven enzalutamide resistance (8). While the underlying radiobiological mechanisms instigating PSMA down-regulation during treatment and in recurrent tumors could be different, these observations could potentially explain the reduced treatment efficacy noted upon repeated PSMA-targeted RIT and radioligant therapy (5, 35, 36). Although preclinical models have limitations, the present outcome demonstrates efficacy of serial [^{225}Ac]hu11B6 treatment in a mouse model; relapsing tumors in mice express abundant levels of hK2 (KLK2) (SI Appendix, Fig. S3) and were successfully treated by a second activity. Furthermore, more than a year after treatment no imminent organ toxicities were noted at necropsy.

Levels of hK2 in the models used in this study were similar to all currently available preclinical PCa models, and about 50-fold lower than in human prostate tissues. Although improved animal models are needed, our results demonstrate that hu11B6 has the capacity to target tissues with low AR and hK2 expression, which is commonly seen in poorly differentiated and late-stage disease.

In addition to deregulated AR regulated genes, further analysis of the transcriptome of relapsing tumors revealed an intriguing profile. Among the most strongly up-regulated genes were ETV1, MMP7, TMEFF2, SCHLAP1, and NTS. ETV1 predisposes prostate cells for cooperation with other oncogenic events, such as PTEN loss, leading to more aggressive disease in murine models and human patients (37). ETV1 expression is associated with enrichment of steroid hormone biosynthesis pathway and androgen and estrogen metabolism by binding to HSD17B7, a gene shared by steroid biosynthesis and steroid hormone biosynthesis pathways. In accordance with this,

we found HSD17B7 to be significantly up-regulated in [^{225}Ac]hu11B6 resistant tumors ($P = 2.27 \times 10^{-7}$). MMP7 is a tumor biomarker associated with increased risk for metastases and poor survival, including PCa (38). TMEFF2 has been reported as an AR-regulated protein (39) that can function both as an oncogene and as a tumor suppressor by affecting Akt and ERG activation (40). While the full-length intracellular TMEFF2 acts as a tumor suppressor (41–43), the shed ectodomain promotes growth (42). Successful immuno-targeting of TMEFF2-expressing PCa tumors has been reported and applied for both positron emission tomography-imaging and antibody-drug conjugates (44, 45). Therefore, in vivo imaging and cotreatment with TMEFF2-targeted compounds could be a potential option to monitor resistance and increase therapeutic efficacy of molecularly targeted α-therapy. Similarly, NTS-based radioligands have been developed for theranostic use (46). NTS/NTS receptor signaling has, among others, been associated with PCa exhibiting neuroendocrine features, such as down-regulation or loss of AR and PSA (47, 48). Thus, NTS-based imaging and therapy may be an option to monitor transition to this very aggressive phenotype and to complement [^{225}Ac]hu11B6 RIT. Finally, SCHLAP1 has been shown to be a reliable biomarker strongly associated with a shorter time to metastatic progression, biochemical relapse, and PCa-specific mortality (49–51). These data together show that while the generalizability of our present findings is limited by the small numbers of tumors ($n = 3$ per group) from a single mouse model, this report on radio-biological mechanisms associated with relapse after α-RIT that could appropriate combination therapies is unique.

The field of molecularly targeted α-therapy is currently undergoing clinical translation, including a planned [^{225}Ac]hu11B6 trial. In the present study, we built on previous preclinical studies of hK2-targeted RIT by investigating novel methods to enhance therapeutic efficacy and explore prospective treatment strategies. To the best of our knowledge, this study showing that FcRn-optimized IgG$_3$ subforms can be applied to RIT is unique.

Table 3. Top 10 down-regulated genes at relapse after treatment with [^{225}Ac]hu11B6-IgG$_1$

Gene name	Fold-change (log$_2$)	P value	Adjusted P value
LAMC3	−8.12	8.02×10^{-232}	2.55×10^{-228}
NES	−6.743	1.08×10^{-205}	2.19×10^{-202}
PASD1	−11.43	4.53×10^{-155}	5.30×10^{-152}
DENND2D	−7.54	3.34×10^{-153}	3.71×10^{-150}
NRXN1	−6.45	1.60×10^{-142}	1.31×10^{-139}
KCNJ3	−4.73	5.93×10^{-136}	4.39×10^{-133}
PTGFR	−6.38	1.50×10^{-132}	1.07×10^{-129}
SLC25A43	−10.94	2.87×10^{-122}	1.72×10^{-119}
FAM213A	−4.92	2.97×10^{-119}	1.74×10^{-116}
SLC7A5	−4.24	5.65×10^{-114}	3.14×10^{-111}

Although further studies are needed to replicate our findings, we also discovered a constellation of putative biomarkers associated with resistance to α-RIT.

Methods

Reagents and Cell Culture. Reagents were purchased from Sigma-Aldrich unless otherwise noted. Cell growth media were obtained from the Media Preparation Core Facility at the Memorial Sloan Kettering Cancer Center (MSKCC, New York, NY). LNCaP-AR (LNCaP cell line with overexpression of wild-type AR and luciferase under the control of the ARR2-Pb promoter) was a kind gift from the laboratory of Charles Sawyers, MSKCC, New York, NY, which previously developed and reported the cell line (52). PC3 was purchased from the American Type Culture Collection (ATCC). All cell lines were cultured according to the developer's instructions and regularly tested for mycoplasma.

Antibodies. Hu11B6-IgG$_1$, hu11B6-IgG$_3^{R435H}$, hu11B6-IgG$_3$, and hu11B6-IgG$_1^{H435A}$ used for an Actinium-225–labeling protocol using two steps developed by Diaprost AB and produced by Innovagen AB. Pre DOTA-conjugated hu11B6-IgG$_1$ applicable for a one-step labeling protocol was developed by Diaprost AB and produced by Fuji-Biosyth.

Radiochemistry. Carrier-free solid ^{225}Actiniumnitrate (5.80×10^4 Ci/g; 214.6×10^4 GBq/g; Oak Ridge National Laboratory) was assayed at secular equilibrium with a CRC-15R radioisotope calibrator (Capintec). All reagents were American Chemical Society reagent grade or better. Radiolabeling procedures were performed using sterile metal-free and pyrogen-free plasticware (Corning). The radiometal chelate DOTA was conjugated to the hu11B6 antibody to yield DOTA-hu11B6 and radiolabeled in one step, as previously described (53). Briefly, 0.005 mL of ^{225}Ac-nitrate dissolved in 0.2 M HCl (Fisher Scientific) (0.1 mCi; 3.7 MBq) was mixed with 1.0 to 1.5 mg of DOTA-hu11B6- IgG$_1$ and buffered with 0.1 mL of 2 M tetramethylammonium acetate and 0.01 mL of 150 g/L of L-ascorbic acid to pH 5.5. The clear and colorless reaction mixture was heated at 37 °C for 75 to 110 min. The reaction was quenched with 0.02 mL of 50 mM diethylenetriaminepentaacetic acid and purified via size-exclusion chromatography using a Bio-Rad 10DG column stationary phase with a 1% human serum albumin (HSA, Swiss Red Cross) and 0.9% sodium chloride (normal saline solution, Abbott Laboratories) mobile phase. Four combinations of native and mutated IgG$_1$ and IgG$_3$ isoforms of hu11B6 (i.e., native IgG$_1$, H435A mutant IgG$_1$, wild-type IgG$_3$, and R435H mutant IgG$_3$) were ^{225}Ac-radiolabeled using a previously described two-step method to prepare α-emitting nanogenerators (19). Radiochemical purity was determined by instant TLC using silica gel-impregnated paper (Gelman Science) using two mobile phases. Mobile phase I was 10 mM ethylenediamine tetraacetic acid; mobile phase II was 9% sodium chloride/10 mM sodium hydroxide. Activity was measured at secular equilibrium using a Packard γ-counter to count the signal in the 370- to 510-keV energy window. The binding kinetics of native [^{225}Ac]DOTA-hu11B6, DOTA-hu11B6, and hu11B6 against recombinant hK2 analyte was measured by surface plasmon resonance using a Biacore 2000 (GE Healthcare), as previously described (3). Antibodies and constructs were captured on a Protein A sensor chip (GE Healthcare). Antibody capture was performed by diluting each sample to a concentration of 0.001 mg/mL in HBS-EP buffer (BR100188, GE Healthcare), and flowing the solution over a protein A sensor chip for 1 min at a flow rate of 0.005 mL/min. Binding kinetics of antibodies were evaluated across a concentration range of hK2 (0, 3.125, 6.25, 12.5, 25, 50, 100, and 200 nM) in HBS-EP buffer. The kinetic data were analyzed with Biacore 3.2.

Animal Studies. For xenograft studies, male athymic BALB/c nude mice [NU(NCr)-*Foxn1^{nu}*; 6- to 8-wk-old, 20 to 25 g] were obtained from Charles River. LNCaP-AR tumors were induced in the left and right flanks by subcutaneous injection of 1 to 5×10^6 cells in a 200-μL cell suspension of a 1:1 (vol/vol) mixture of medium with Matrigel (Collaborative Biomedical Products). Tumors developed after ~3 to 7 wk. The previously developed Hi-*Myc* × pb_*KLK2_* Hi-*Myc* GEMM, a PCa-susceptible transgenic mouse model prostate tissue-specific hK2 expression, was used in the studies (10). All interventions were performed under anesthesia (2% isoflurane).

Pharmacokinetic Tissue Distribution. Biodistribution studies were conducted to investigate uptake and pharmacokinetic distribution of various Actinium-225 labeled IgG-subclasses (IgG$_1$, IgG$_1^{H435A}$, IgG$_3$, IgG$_3^{R435H}$) of hu11B6 ([^{225}Ac]hu11B6) in the GEMM model, and LNCaP-AR and PC3 xenografts. Mice received a single 300 nCi (11 kBq) activity of [^{225}Ac]hu11B6-IgG$_1$, [^{225}Ac]

hu11B6^{R435H}, [^{225}Ac]hu11B6-IgG$_1$, or [^{225}Ac]hu11B6-IgG$_1^{R435H}$ (300 nCi on 5 μg antibody). Radioimmuno-compounds were administered via intravenous tail-vein injection ($t = 0$ h). Animals ($n = 4$ to 5 per group) were killed by CO$_2$ asphyxiation at 4, 48, 120, and 360 hpi. Blood was immediately harvested by cardiac puncture. Tissues (including the tumor) were removed, rinsed in water, dried on paper, weighed, and counted on a γ-counter using a 370- to 510-keV energy window at secular equilibrium. Aliquots (0.020 mL) of the injected activities were used as decay correction standards and background signal was subtracted from each sample. The percentage of IA/g was calculated for each animal and data plotted as mean ± SD.

Therapy Studies. In the initial studies, the therapeutic efficacies of 300 nCi (11 kBq) [^{225}Ac] on 5 μg hu11B6-IgG$_1$, hu11B6-IgG$_1^{H435A}$, hu11B6-IgG$_3$, and hu11B6IgG$_3^{R435H}$, labeled using a two-step protocol, were compared in subcutaneous LNCaP-AR tumors and GEMM. In a subsequent study, two different treatment regimens of labeled hu11B6-IgG$_1$, labeled using a one-step protocol, were evaluated; single activity treatment (600 nCi; 22 kBq) was compared to fractionated administration (300 + 300 nCi; 11 + 11 kBq) [^{225}Ac]hu11B6-IgG$_1$ in subcutaneous LNCaP-AR tumors (five mice per treatment group and five untreated mice per treatment group). Length (l) and width (w) of the tumors were measured by caliper and tumor volume was calculated using the modified formula for a rotated ellipsoid ($V = 1/2\ w^2 l$) was calculated. Weight loss of 20% or a tumor diameter exceeding 15 mm was set as an endpoint. Survival percentages over time were calculated to study therapy effectiveness in both studies.

Measurement of Kallikreins. Free (fPSA) and total (tPSA) PSA were determined with the dual-label DELFIA immunofluorometric assay (Prostatus PSA Free/Total PSA from Perkin-Elmer Life Sciences). This assay determines free and complexed PSA in an equimolar fashion, and the cross-reaction for PSA-α 1-antichymotrypsin (PSA-ACT) in the fPSA assay was below 0.2% (54). The lower limit of detection for tPSA was 0.10 ng/mL (coefficient of variation of 5.0% at 2.32 ng/mL) and for fPSA 0.04 ng/mL (coefficient of variation of 5.9% at 0.25 ng/mL). hK2 was measured using an in-house research assay protocol (55); the detection limit of the assay was 0.005 ng/mL with assay imprecision values (mean coefficients of variation) ranging from 5.7 to 11% for high and low hK2 controls, respectively.

RNA Extraction. RNA from snap-frozen LNCaP-AR tumors was extracted using the RNeasy Mini Kit (Qiagen) according to the instructions provided by the manufacturer.

Transcriptome Sequencing (RNA Sequencing). After RiboGreen quantification and quality control by Agilent BioAnalyzer, 500 ng of total RNA underwent polyA selection and TruSeq library preparation according to instructions provided by Illumina (RS-122-2102, TruSeq Stranded mRNA LT Kit) with eight cycles of PCR. Samples were barcoded and run on a HiSEq. 4000 in a 50-bp/50-bp paired-end run, using the HiSEq. 3000/4000 Sequencing by Synthesis Kit (Illumina). An average of 44 million paired reads was generated per sample. Ribosomal reads represented maximally 1.2% of the reads generated and the percent of mRNA bases averaged 63%.

Transcriptome Sequencing Analysis. Raw read count RNA-sequencing gene expression data for a total of 58,828 genes were acquired from tumor samples treated with 2× 300 nCi (2× 11 kBq) [^{225}Ac]hu11B6-IgG$_1$ ($n = 3$) and left untreated ($n = 3$). After confirming the quality of sequences via FastQC, principal component analysis (PCA) was performed in R, where the PCA plot demonstrated a clear division between the samples from the two cohorts (*SI Appendix*, Fig. S5). Hierarchical clustering of samples using the Manhattan method for distance calculation further demonstrated a clear divide between the two cohorts. To visualize the magnitude of effect and to highlight the groups of genes that were similar to each other based on their expression, a heatmap was plotted based on the log$_2$ raw read counts (*SI Appendix*, Fig. S6).

Differential expression analysis of RNA-sequencing expression profiles was performed using Bioconductor's edgeR package in R. edgeR implements statistical methods based on negative binomial distributions, namely empirical Bayes methods, that permit the estimation of gene-specific biological variation, even for experiments with minimal levels of biological replication. Raw read counts are provided as input where edgeR introduces possible bias sources into the statistical model to perform an integrated normalization followed by differential expression analysis. P values and fold-change in log$_2$ were calculated for each gene. P values were adjusted for false-discovery rate (10% cutoff) using the Benjamini–Hochberg method. DEGs were then selected based on the following criteria: Adjusted $P < 0.001$ and absolute

MEDICAL SCIENCES

www.manaraa.com

value of $\log_2$ fold-change > 2. A positive fold-change represented up-regulation, whereas a negative fold-change represented down-regulation in tumor samples treated with [^{225}Ac]hu11B6-IgG[1].

Statistics. All statistical analysis of data, except for analysis of RNA-sequencing data (see above), was performed using Prism software (Graphpad Software). Data are represented as mean $\pm$ SD or median and range (survival data) ($n \geq$ 3 independent samples per group for all analyses). No datapoints were excluded from analysis. Unpaired, two-tailed t tests were used for comparison of two groups. Analysis of survival data were performed by the log-rank test (Mantel–Cox). A $P < 0.05$ was considered to indicate statistical significant differences.

Ethical Approval. All animal experiments were conducted in compliance with institutional Animal Care and Use Committee-established guidelines at MSKCC and under supervision by the MSKCC Research Animal Resource Center.

Data Availability Statement. The Gene Expression Omnibus database accession number for RNA sequencing data reported in this paper is GSE147850.

1. C. Kratochwil et al., Targeted alpha therapy of mCRPC with (225)Actinium-PSMA-617: Swimmer-plot analysis suggests efficacy regarding duration of tumor-control. J. Nucl. Med. **59**, 795–802 (2018).
2. M. Sathekge et al., Predictors of overall and disease free survival in metastatic castration-resistant prostate cancer patients receiving (225)Ac-PSMa-617 radioligand therapy. J. Nucl. Med. **61**, 62–69 (2020).
3. M. R. McDevitt et al., Feed-forward alpha particle radiotherapy ablates androgen receptor-addicted prostate cancer. Nat. Commun. **9**, 1629 (2018).
4. C. Kratochwil et al., Targeted α-therapy of metastatic castration-resistant prostate cancer with ^{225}Ac-PSMA-617: Dosimetry estimate and empiric dose finding. J. Nucl. Med. **58**, 1624–1631 (2017).
5. M. J. Evans et al., Noninvasive measurement of androgen receptor signaling with a positron-emitting radiopharmaceutical that targets prostate-specific membrane antigen. Proc. Natl. Acad. Sci. U.S.A. **108**, 9578–9582 (2011).
6. T. A. Hope et al., 68Ga-PSMA-11 PET imaging of response to androgen receptor inhibition: First human experience. J. Nucl. Med. **58**, 81–84 (2017).
7. M. C. Hupe et al., Expression of prostate-specific membrane antigen (PSMA) on biopsies is an independent risk stratifier of prostate cancer patients at time of initial diagnosis. Front. Oncol. **8**, 623 (2018).
8. V. K. Arora et al., Glucocorticoid receptor confers resistance to antiandrogens by bypassing androgen receptor blockade. Cell **155**, 1309–1322 (2013).
9. D. L. J. Thorek et al., Harnessing androgen receptor pathway activation for targeted alpha particle radioimmunotherapy of breast cancer. Clin. Cancer Res. **25**, 881–891 (2019).
10. D. L. Thorek et al., Internalization of secreted antigen-targeted antibodies by the neonatal Fc receptor for precision imaging of the androgen receptor axis. Sci. Transl. Med. **8**, 367ra167 (2016).
11. O. Vilhelmsson Timmermand, E. Larsson, D. Ulmert, T. A. Tran, S. Strand, Radio-immunotherapy of prostate cancer targeting human kallikrein-related peptidase 2. EJNMMI Res. **6**, 27 (2016).
12. O. V. Timmermand et al., Preclinical imaging of kallikrein-related peptidase 2 (hK2) in prostate cancer with a (111)In-radiolabelled monoclonal antibody, 11B6. EJNMMI Res. **4**, 51 (2014).
13. W. P. Burmeister, A. H. Huber, P. J. Bjorkman, Crystal structure of the complex of rat neonatal Fc receptor with Fc. Nature **372**, 379–383 (1994).
14. J. G. Salfeld, Isotype selection in antibody engineering. Nat. Biotechnol. **25**, 1369–1372 (2007).
15. A. Natsume et al., Engineered antibodies of IgG1/IgG3 mixed isotype with enhanced cytotoxic activities. Cancer Res. **68**, 3863–3872 (2008).
16. P. Bruhns et al., Specificity and affinity of human Fcgamma receptors and their polymorphic variants for human IgG subclasses. Blood **113**, 3716–3725 (2009).
17. J. G. Jurcic, Targeted alpha-particle therapy for hematologic malignancies. J. Med. Imaging Radiat. Sci. **50** (suppl. 1), S53–S57 (2019).
18. M. R. McDevitt, D. Ma, J. Simon, R. K. Frank, D. A. Scheinberg, Design and synthesis of 225Ac radioimmunopharmaceuticals. Appl. Radiat. Isot. **57**, 841–847 (2002).
19. M. R. McDevitt et al., Tumor therapy with targeted atomic nanogenerators. Science **294**, 1537–1540 (2001).
20. R. M. Väänänen et al., Cancer-associated changes in the expression of TMPRSS2-ERG, PCA3, and SPINK1 in histologically benign tissue from cancerous vs noncancerous prostatectomy specimens. Urology **83**, 511.e1-511.e7 (2014).
21. R. M. Väänänen et al., Association of transcript levels of 10 established or candidate-biomarker gene targets with cancerous versus non-cancerous prostate tissue from radical prostatectomy specimens. Clin. Biochem. **46**, 670–674 (2013).
22. D. Ulmert, R. J. Klein, Genetic signature of prostate cancer mouse models resistant to optimized hK2 targeted alpha-particle therapy. Gene Expression Omnibus. https://www.ncbi.nlm.nih.gov/geo/query/acc.cgi?acc=GSE147850. Deposited 31 March 2020.
23. H. I. Scher et al.; AFFIRM Investigators, Increased survival with enzalutamide in prostate cancer after chemotherapy. N. Engl. J. Med. **367**, 1187–1197 (2012).
24. J. S. de Bono et al.; COU-AA-301 Investigators, Abiraterone and increased survival in metastatic prostate cancer. N. Engl. J. Med. **364**, 1995–2005 (2011).
25. B. Burnette, R. R. Weichselbaum, Radiation as an immune modulator. Semin. Radiat. Oncol. **23**, 273–280 (2013).
26. N. M. Stapleton et al., Competition for FcRn-mediated transport gives rise to short half-life of human IgG3 and offers therapeutic potential. Nat. Commun. **2**, 599 (2011).
27. R. Jefferis, Antibody therapeutics: Isotype and glycoform selection. Expert Opin. Biol. Ther. **7**, 1401–1413 (2007).
28. W. K. Weng, R. Levy, Two immunoglobulin G fragment C receptor polymorphisms independently predict response to rituximab in patients with follicular lymphoma. J. Clin. Oncol. **21**, 3940–3947 (2003).
29. F. Nimmerjahn, P. Bruhns, K. Horiuchi, J. V. Ravetch, FcgammaRIV: A novel FcR with distinct IgG subclass specificity. Immunity **23**, 41–51 (2005).
30. A. M. Wu, Engineered antibodies for molecular imaging of cancer. Methods **65**, 139–147 (2014).
31. S. Bournazos, T. T. Wang, R. Dahan, J. Maamary, J. V. Ravetch, Signaling by antibodies: Recent progress. Annu. Rev. Immunol. **35**, 285–311 (2017).
32. T. R. Simpson et al., Fc-dependent depletion of tumor-infiltrating regulatory T cells co-defines the efficacy of anti-CTLA-4 therapy against melanoma. J. Exp. Med. **210**, 1695–1710 (2013).
33. C. Twyman-Saint Victor et al., Radiation and dual checkpoint blockade activate non-redundant immune mechanisms in cancer. Nature **520**, 373–377 (2015).
34. O. V. Timmermand et al., Preclinical efficacy of hK2 targeted [^{177}Lu]hu11B6 for prostate cancer theranostics. Theranostics **9**, 2129–2142 (2019).
35. A. Gafita et al., Early experience of rechallenge ^{177}Lu-PSMA radioligand therapy after an initial good response in patients with advanced prostate cancer. J. Nucl. Med. **60**, 644–648 (2019).
36. A. Afshar-Oromieh et al., Repeated PSMA-targeting radioligand therapy of metastatic prostate cancer with ^{131}I-MIP-1095. Eur. J. Nucl. Med. Mol. Imaging **44**, 950–959 (2017).
37. E. Baena et al., ETV1 directs androgen metabolism and confers aggressive prostate cancer in targeted mice and patients. Genes Dev. **27**, 683–698 (2013).
38. M. Ii, H. Yamamoto, Y. Adachi, Y. Maruyama, Y. Shinomura, Role of matrix metalloproteinase-7 (matrilysin) in human cancer invasion, apoptosis, growth, and angiogenesis. Exp. Biol. Med. (Maywood) **231**, 20–27 (2006).
39. R. F. Overcash et al., Androgen signaling promotes translation of TMEFF2 in prostate cancer cells via phosphorylation of the α subunit of the translation initiation factor 2. PLoS One **8**, e55255 (2013).
40. X. Chen, M. J. Ruiz-Echevarría, TMEFF2 modulates the AKT and ERK signaling pathways. Int. J. Biochem. Mol. Biol. **4**, 83–94 (2013).
41. S. Gery, C. L. Sawyers, D. B. Agus, J. W. Said, H. P. Koeffler, TMEFF2 is an androgen-regulated gene exhibiting antiproliferative effects in prostate cancer cells. Oncogene **21**, 4739–4746 (2002).
42. X. Chen et al., The tumor suppressor activity of the transmembrane protein with epidermal growth factor and two follistatin motifs 2 (TMEFF2) correlates with its ability to modulate sarcosine levels. J. Biol. Chem. **286**, 16091–16100 (2011).
43. T. Green, X. Chen, S. Ryan, A. S. Asch, M. J. Ruiz-Echevarría, TMEFF2 and SARDH co-operate to modulate one-carbon metabolism and invasion of prostate cancer cells. Prostate **73**, 1561–1575 (2013).

Bicak et al.

www.manaraa.com

44. S. P. Williams *et al.*, ImmunoPET helps predicting the efficacy of antibody-drug conjugates targeting TENB2 and STEAP1. *Oncotarget* **7**, 25103–25112 (2016).
45. C. A. Boswell *et al.*, Differential effects of predosing on tumor and tissue uptake of an 111In-labeled anti-TENB2 antibody-drug conjugate. *J. Nucl. Med.* **53**, 1454–1461 (2012).
46. J. Schulz *et al.*, Proof of therapeutic efficacy of a ^{177}Lu-labeled neurotensin receptor 1 antagonist in a colon carcinoma xenograft model. *J. Nucl. Med.* **58**, 936–941 (2017).
47. E. G. Bluemn *et al.*, Androgen receptor pathway-independent prostate cancer is sustained through FGF signaling. *Cancer Cell* **32**, 474–489.e6 (2017).
48. W. Abida *et al.*, Genomic correlates of clinical outcome in advanced prostate cancer. *Proc. Natl. Acad. Sci. U.S.A.* **116**, 11428–11436 (2019).
49. J. R. Prensner *et al.*, RNA biomarkers associated with metastatic progression in prostate cancer: A multi-institutional high-throughput analysis of SChLAP1. *Lancet Oncol.* **15**, 1469–1480 (2014).
50. R. Mehra *et al.*, Overexpression of the long non-coding RNA SChLAP1 independently predicts lethal prostate cancer. *Eur. Urol.* **70**, 549–552 (2016).
51. M. L. K. Chua *et al.*, A prostate cancer "nimbosus": Genomic instability and SChLAP1 dysregulation underpin aggression of intraductal and cribriform subpathologies. *Eur. Urol.* **72**, 665–674 (2017).
52. C. D. Chen *et al.*, Molecular determinants of resistance to antiandrogen therapy. *Nat. Med.* **10**, 33–39 (2004).
53. W. F. Maguire, M. R. McDevitt, P. M. Smith-Jones, D. A. Scheinberg, Efficient 1-step radiolabeling of monoclonal antibodies to high specific activity with 225Ac for α-particle radioimmunotherapy of cancer. *J. Nucl. Med.* **55**, 1492–1498 (2014).
54. T. Piironen *et al.*, Immunofluorometric assay for sensitive and specific measurement of human prostatic glandular kallikrein (hK2) in serum. *Clin. Chem.* **42**, 1034–1041 (1996).
55. V. Väisänen *et al.*, Development of sensitive immunoassays for free and total human glandular kallikrein 2. *Clin. Chem.* **50**, 1607–1617 (2004).

MEDICAL SCIENCES

Bicak et al.

www.manaraa.com